
ORIGINAL ARTICLE

Special Issue: High-Performance Power Converters for Renewable Energies and Electrical Vehicle Application

Performance Evaluation for an Hourglass-Shaped Impedance-Network-Based High Step-up Converter in a PV System Using PSIM[®] Simulation

Abdelali El Aroudi¹ | Guidong Zhang² | Mohamed Al-Numay²

¹Department of Electroics, Electrical Engineering and Automatic Control, Universitat Rovira i Virgili, Tarragona, Spain

²School of Automation, Guangdong University of Technology, Guangzhou, China

³Electrical Engineering Department, King Saud University, Riyadh, Saudi Arabia

Correspondence

Abdelali El Aroudi, Department of Electronics, Electrical Engineering and Automatic Control, Universitat Rovira i Virgili, Tarragona, 43007, Spain
Email: abdelali.elaroudi@urv.cat

Funding information

This work was supported by the Spanish *Ministerio de Economía y Competitividad* under grants DPI2017-84572-C2-1-R. A. El Aroudi and M. Al-Numay extend their appreciation to the International Scientific Partnership Program ISPP at King Saud University for funding this research work through ISPP#00102.

In this paper, the control design and the performance evaluation of a novel high-step-up converter with a hourglass-shaped impedance network (HIN) are performed when used as an interface between a PV source and a load in a PV system. For optimum energy extraction from the PV source, the PV voltage controller design and optimization to track the maximum power point of the PV system is addressed. The converter offers the possibility of an optimum regulation of the PV voltage with voltage mode control using a simple type-III compensation network resulting in a low overshoot, a relatively short settling time and negligible energy loss after a change of input reference due to the maximum power point tracking (MPPT) or to irradiance change. To evaluate the performance of the HIN converter when used in a PV system PSIM[®] software is used to perform numerical simulations using the switched model under different conditions.

Keywords: hourglass-shaped impedance network converter, high voltage gain, PV system, MPPT, control design, simulation.

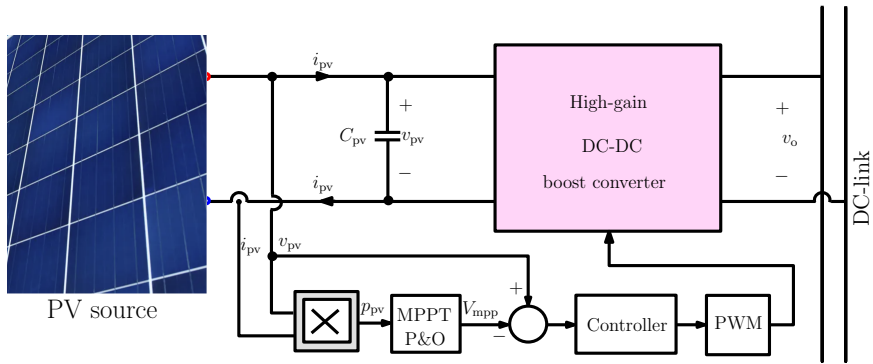


FIGURE 1 Block diagram of a PV system using a high gain boost converter.

1 | INTRODUCTION

In recent years, photovoltaic (PV) energy was developed rapidly as a kind of renewable energy source that is growing in all over the globe. PV energy can be converted to electricity with almost zero emissions and is therefore considered one of the most environmentally-friendly energies. Moreover, PV systems allow to integrate solar energy to the electrical supply and provide consumers with sustainable power. The voltage-current curve of PV energy sources is nonlinear and it changes with weather conditions. This curve has a point called the maximum power point (MPP) at which the system is forced to deliver its maximum power. The voltage coordinate of the MPP lies within the range (15, 42) V for many PV modules. To increase this voltage to a higher usable level, a voltage step-up converter is needed. Hence, a major challenge that needs to be addressed by the power electronics interface is to take the low voltage at the output of the solar PV source and convert it into a much higher voltage level. For that, a high voltage gain converter must be used as an interface. Therefore, to convert the energy supplied by a PV module to the power grid, high-step-up DC-DC converters play a vital role in the energy conversion stage. Different high voltage gain DC-DC converter topologies exist in the literature [1, 2, 3, 4]. Fig. 1 shows a block diagram of a PV system consisting of PV module, a capacitor, an MPPT block to extract the maximum power of the PV module, a PV voltage controller, a PWM and a DC-link output which can be either a battery or another power converter such as a DC-AC inverter.

There are many types of high voltage gain boost converters, but roughly speaking, these topologies can be classified into converters with magnetic coupling or without magnetic coupling [1]. Different kinds of non-coupled-inductor converters have been considered in the past. For example, a high voltage gain converter, using interleaved inductors is proposed in [5]. In [6] a high voltage gain converter based on quadratic boost converter has been proposed. The topology is equipped an additional capacitor-inductor-diode network to reduce voltage stress of switching devices. Authors in [7] presented a power converter with a high voltage gain for fuel cell vehicles based on a combined boost-Ćuk topology. In [8, 9, 10] the authors proposed high voltage gain multi-cell boost converters. The other type of high voltage power converters, the ones with magnetic coupling, can achieve a increased voltage gain by using a high turn ratio in the magnetic coupling [11, 12]. Soft switching techniques can be used in coupled-inductor converters to improve the efficiency [13, 14]. Similar to [12], coupled-inductor converter with interleaving effect and low input current ripple and voltage stress in the components has been proposed in [15, 16].

Since the introduction of the Z-source converter in [17], impedance network topologies have attracted a lot of interests and many of such topologies have been proposed for several applications such as in electric vehicle battery

charging, renewable energy technologies, motion control and distributed generation systems among others. These topologies are all characterized by a high voltage gain making them suitable in this kind of applications. Different basic and improved impedance network converter topologies exist in the literature [18]. These include impedance network converters with magnetically coupled inductors [19, 20], trans-Z-source [21], TZ-source [22], LCCT-Z-source [23], Γ -source [24], T-source [25], Y-source [26] and A-source [27] among others. Apart from the high voltage boosting capability, other factors must be considered if these converters are to be used in renewable energy applications such as in PV systems. In particular, the existence of an inductor at the input port of the converter is one of the requirements to perform MPPT at this port. This is because pulsating current is not suitable in this kind of applications and an input filter is then necessary for converters not having this inductor at the input port. Additional filtering elements increase the losses, size, component count and cost. Moreover, the previous topologies have some additional practical issues. For example, regardless of the use or not of coupled-inductors, electrolytic capacitors (ECs) are the most critical components in power converters. The lifetime of these ECs is shorter than other components due to the voltage spikes in practical energy conversion systems. Besides, ECs are bulky and they reduce the power density of the system. Moreover, ECs suffer from safety issues since they can explode. Therefore, in practice, the use of ECs is expected to be limited in many applications. To remedy the previous issues, a non-ECs high-step-up hourglass impedance network (HIN) converter with a high power density was proposed in [28] where the steady-state analysis of the converter has been performed by considering an ideal constant input voltage. The control design of the HIN converter and its performance evaluation when used in a PV system with a nonlinear PV source have not been addressed. In this paper a control oriented approach is followed to derive a small signal model for the PV-fed HIN converter from the switched model using PSIM[®] software [29]. Based on the switched model, the control design of the PV voltage is addressed. The performances of the converter when used in a PV system performing MPPT are evaluated.

The structure of this paper is as follows. After this introduction, in Section 2, the high voltage gain HIN converter will be described and its operation principle will be explained. The steady-state performances of the converter are addressed in Section 3. The small signal modeling and the controller design for regulating the input voltage of the converter when this is used for MPPT is addressed in Section 4 using the `SmartCtrl` tool of PSIM[®]. In Section 5 it is shown that the HIN converter could be an excellent candidate for simple MPPT tracking in PV systems requiring high voltage gain. Finally, conclusions of this study are summarized in the last section.

2 | OPERATION PRINCIPLE OF THE HIN HIGH STEP-UP CONVERTER IN A PV SYSTEM

The HIN converter in a PV system is shown in Fig. 2. The converter is supplied from a PV energy source for performing MPPT and is feeding a resistive load. The HIN network has two inductors with inductance values L_1 and L_2 , two capacitors C_1 and C_2 , two diodes D_1 , D_2 and a switch S_1 . Other components of the HIN topology are the diodes D_3 and D_4 and the switch S_2 and the two output capacitors with capacitance values C_3 and C_4 . Compared to existing impedance networks in the literature, the HIN has a lower capacitor voltage stress and higher voltage gain as will be shown later. The input voltage control system of the converter uses a two zeros (with three poles) compensation scheme based on a type-III controller and the reference voltage for this controller is provided by a MPPT block based on the Perturb and Observe algorithm. A comparator compares the control signal provided by the controller with an external periodic ramp voltage with amplitude V_M and period T_s (frequency f_s). The output of the comparator decides the states of both switches S_1 and S_2 . Similar to other power converter topologies, the HIN converter can operate in both continuous conduction mode (CCM) and discontinuous conduction mode (DCM). Since the CCM is usually preferred

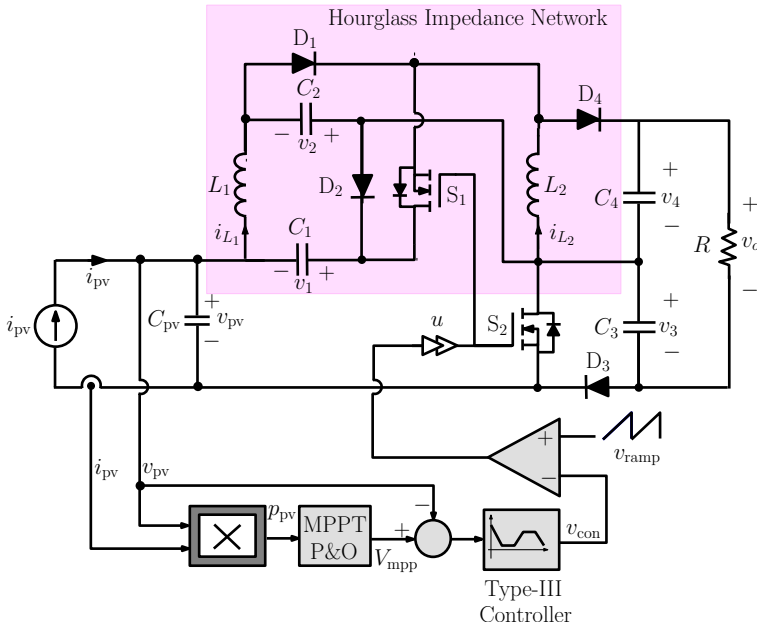


FIGURE 2 Circuit schematic diagram of the high voltage gain HIN boost converter under a type-II PV voltage mode control.

in PV applications, this mode is considered in this paper. The CCM is characterized by two different configurations whose circuit diagrams are shown in Fig. 3 where the state of the switching elements are indicated.

In this study, the steady-state analysis and the control are based on the following assumptions are made

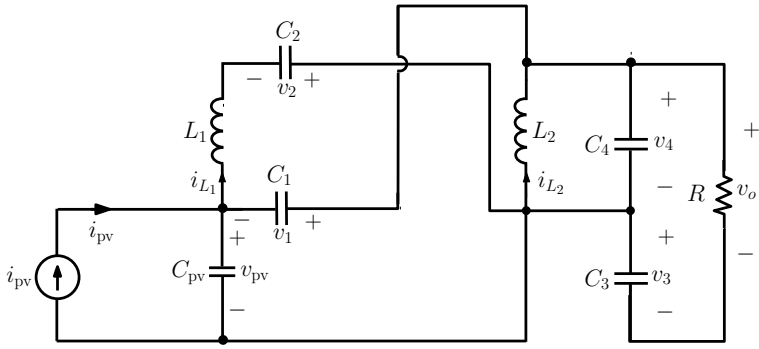
1. All reactive components are ideal and therefore their losses are neglected.
2. All diodes are ideal and therefore their capacitance, their forward voltage and ON resistance are neglected.
3. The transistors are ideal and therefore their ON resistance and parasitic inductance and capacitance are also ignored.
4. All capacitors are large enough that the voltage across each one of them is considered constant during each subinterval.

It is worth noting that when operating **Mode 1** takes place the current flows from inductor L_1 to L_2 through capacitors C_1 and C_2 ; and when operating **Mode 2** occurs, the current flows back.

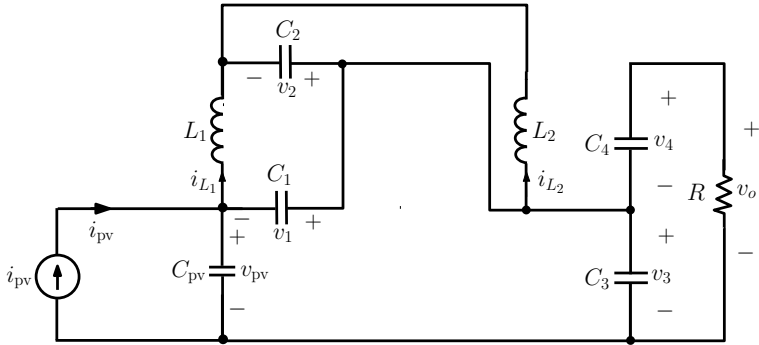
3 | STEADY-STATE ANALYSIS OF THE HIN CONVERTER IN A PV SYSTEM

3.1 | Steady-state voltage stress in the capacitors and conversion voltage gain

The used type-III controller for the HIN converter has a pole at the origin with which the average value of the input PV voltage v_{pv} in steady-state is equal to its desired reference V_{mpp} dictated by the MPPT controller. The steady-state



(a) **Mode 1:** Switches S_1 , S_2 and diode D_4 are ON and diodes D_1 , D_2 and D_3 are OFF



(b) **Mode 2:** Switches S_1 , S_2 and diodes D_4 are OFF and diodes D_1 , D_2 and D_3 are ON.

FIGURE 3 Circuit diagrams corresponding to (a) **Mode 1** and (b) **Mode 2**.

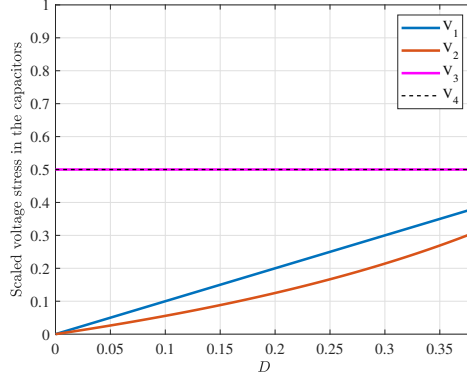


FIGURE 4 Voltage stresses scaled by the output voltage V_o for the different capacitors of the HIN converter.

values of the other capacitor voltages can be obtained by applying volt-second balance principle to the inductors L_1 and L_2 . This leads to the following expressions for the steady-state values of the capacitor and the output voltages (see [28] for more details)

$$\begin{cases} V_1 = \left(\frac{D(2-D)V_{mpp}}{D^2-3D+1} \right), \\ V_2 = \frac{DV_{mpp}}{D^2-3D+1}, \\ V_3 = \frac{(1-D)V_{mpp}}{D^2-3D+1}, \\ V_4 = \frac{(1-D)V_{mpp}}{D^2-3D+1}, \\ V_o = \frac{2(1-D)V_{mpp}}{D^2-3D+1}. \end{cases} \quad (1)$$

Note that the voltage stress of the output capacitor in a conventional boost converter is the output voltage. By scaling the previous the steady-state average values of the capacitor voltages V_1, V_2, V_3, V_4 with respect the the output voltage V_o one gets

$$\begin{cases} \frac{V_1}{V_o} = D, \\ \frac{V_2}{V_o} = \frac{D}{2(1-D)}, \\ \frac{V_3}{V_o} = \frac{V_4}{V_o} = \frac{1}{2}. \end{cases} \quad (2)$$

In Fig. 4, capacitor voltage stress from (2) scaled by the output voltage are shown as functions of the operating duty cycle D . It is worth noticing that the voltage stress V_1, V_2, V_3 and V_4 , of capacitors C_1, C_2, C_3 and C_4 is smaller than the output voltage within the entire operating range of duty cycle values. The bigger voltage stress is one half the output voltage and it corresponds to the capacitors C_3 and C_4 .

From the last equation in (2), the conversion ratio of the HIN converter can be expressed as follows

$$M(D) = \frac{V_o}{V_{mpp}} = \frac{2(1-D)}{D^2 - 3D + 1}. \quad (3)$$

where V_o is the output voltage and the V_{mpp} is the MPP voltage.

3.2 | Steady-state inductor currents

The steady-state average values of the inductor currents I_1 and I_2 and their ripple amplitudes Δi_1 and Δi_2 can be obtained by applying charge balance principle to the capacitors C_1 and C_2 , hence obtaining the following expressions

$$\left\{ \begin{array}{l} I_1 = \frac{2(1-D)}{D^2 - 3D + 1} \frac{V_o}{R}, \\ I_2 = \frac{2}{D^2 - 3D + 1} \frac{V_o}{R}, \\ \Delta i_1 = \frac{V_{mpp} D (1-D)^2 T_s}{L_1 (D^2 - 3D + 1)}, \\ \Delta i_2 = \frac{V_{mpp} D (1-D) T_s}{L_2 (D^2 - 3D + 1)}. \end{array} \right. \quad (4)$$

where V_o is the output voltage and the R is the load resistance. These expressions will be validated later by using numerical simulations performed using PSIM[®] software.

3.3 | Voltage and current stresses of the electronic devices

Following the same previous steady-state analysis, the voltage stress of the diodes D_1 , D_2 , D_3 and D_4 , namely V_{D_1} , V_{D_2} , V_{D_3} , and switches S_1 and S_2 , namely V_{S_1} and V_{S_2} , can be expressed as follows

$$\left\{ \begin{array}{l} V_{D_1} = \frac{V_{mpp}}{D^2 - 3D + 1}, \\ V_{D_2} = \frac{(1-D)V_{mpp}}{D^2 - 3D + 1}, \\ V_{D_3} = \frac{(1-D)V_{mpp}}{D^2 - 3D + 1}, \\ V_{D_4} = \frac{V_{mpp}}{D^2 - 3D + 1}, \\ V_{S_1} = \frac{DV_{mpp}}{D^2 - 3D + 1}, \\ V_{S_2} = \frac{(1-D)V_{mpp}}{D^2 - 3D + 1}. \end{array} \right. \quad (5)$$

Likewise, the average current I_{D_1} , I_{D_2} and I_{D_3} of the diodes of D_1 , D_2 , D_3 , D_4 and switches S_1 and S_2 can be

written as follow

$$\left\{ \begin{array}{l} I_{D_1} = \frac{2}{D^2 - 3D + 1} \frac{V_o}{R}, \\ I_{D_2} = \frac{7 - 8D}{4(D^2 - 3D + 1)} \frac{V_o}{R}, \\ I_{D_3} = \frac{1}{4(D^2 - 3D + 1)} \frac{V_o}{R}, \\ I_{D_4} = \frac{2}{D} \frac{V_o}{R}, \\ I_{S_1} = \frac{2(1 - D)^2}{D(D^2 - 3D + 1)} \frac{V_o}{R}, \\ I_{S_2} = \frac{2(1 - D)}{D(D^2 - 3D + 1)} \frac{V_o}{R}. \end{array} \right. \quad (6)$$

3.4 | Brief comparison with existing high gain power converters

A detailed comparison between the HIN converter and some high gain power converter topologies from the literature is provided in [28]. Here only a summary of this comparison is provided. Table 1 shows the voltage gain, voltage stress on the main switch of the the HIN converter and the voltage stress on the different capacitors as compared to other power converter topologies including the conventional boost converter. Compared to other converters, the voltage gain of the HIN converter is significantly high even for low values of operating duty cycle. The HIN converter performs better than other high voltage gain converter topologies with regard to the voltage stress on devices. The number of components of the HIN converter is comparable to other converters. However, because of their small capacitance values, the use of electrolytic-less capacitors in the HIN topology allows a smaller size and a higher power density.

Fig. 5 shows the voltage gain corresponding to the converters of Table 1 in terms of the operating duty cycle D . For the HIN converter, a positive output voltage is only obtained with D within the range $(0, 0.38)$. However, ideally, for $D = 1/3$ the voltage gain is already $M(1/3) = 12$. For a fair comparison, the turns ratio of the of the converter with magnetic coupling in [11] is selected as $n_2 = 2$ and the number of cells for the converter in [30] is chosen to be $n_1 = 3$. It can be observed that compared to other converters, the gain of the HIN topology is significantly higher higher than converters in [31, 32] and theoretically reaches a value of around 20 for a duty cycle $D = 0.35$. Compared to the converters in [6, 11, 30, 33], the gain of the HIN topology is higher with the same duty cycle value.

4 | SMALL-SIGNAL MODEL OF THE HIN CONVERTER AND ITS INPUT CONTROLLER DESIGN

4.1 | Modeling of the HIN converter power stage and the PV generator

The frequency response of a system can be obtained by performing AC analysis. The frequency response of the converter power stage has been first obtained by using PSIM[®] software which has the key feature that the AC analysis can be performed using directly the switched model and without requiring to obtain and to use the average model. A small AC sinusoidal signal is injected into the system as perturbation of the duty cycle and the voltage at the PV generator output is measured at the same frequency. The AC sweep process is repeated for 400 points logarithmically

TABLE 1 Comparison of the voltage gain and voltage stress in the components between the HIN converter and other existing high gain power converters

Reference	Voltage gain	Voltage stress on capacitors	Voltage stress on switches
[6]	$M(D) = \frac{1+D}{(1-D)^2}$	$V_1 = \frac{1-D}{1+D}V_o, V_4 = V_o$ $V_2 = V_3 = \frac{V_o}{1+D}$	$V_{S1} = \frac{V_o}{2-D}$
[11]	$M(D) = \frac{1+n_2(1-D)}{1-2D}$	$V_1 = \frac{1-D}{1+n_2(1-D)}V_o$ $V_2 = \frac{D}{1+n_2(1-D)}V_o$ $V_{o1} = \frac{1}{1+n_2(1-D)}V_o$ $V_{o2} = \frac{n_2(1-D)}{1+n_2(1-D)}V_o$	$V_{S1} = \frac{V_o}{1+n_2(1-D)}$
[31]	$M(D) = \frac{1}{1-5D+2D^2}$	$V_1 = 2DV_o, V_2 = (1-2D)V_o$ $V_3 = V_o = V_o$	$V_{S1} = (1-2D)V_o$ $V_{S2} = V_o$
[32]	$M(D) = \frac{1}{1-4D}$	$V_1 = V_2 = 2DV_o$ $V_3 = V_o$	$V_{S1} = V_{S2} = V_o$
[33]	$M(D) = \frac{1}{1-2D}$	$V_1 = \frac{1-2D}{1-D}V_o, V_2 = \frac{D}{1-D}V_o$ $V_o = V_o$	$V_{S1} = (1+D)V_o$
The HIN Converter	$M(D) = \frac{2(1-D)}{1-3D+D^2}$	$V_1 = \frac{2D-D^2}{2(1-D)}V_o, V_2 = \frac{D}{2(1-D)}V_o$ $V_3 = V_4 = \frac{V_o}{2}$	$V_{S1} = \frac{D}{2(1-D)}V_o$ $V_{S2} = \frac{V_o}{2}$

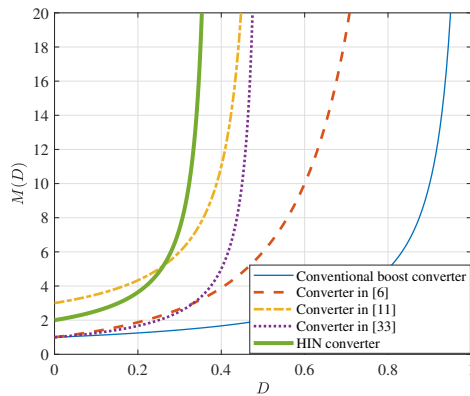


FIGURE 5 Voltage gain for the HIN converter in comparison with other impedance network converters.

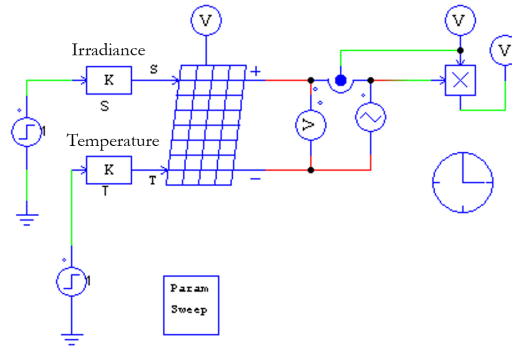


FIGURE 6 The PSIM[®] schematic diagram used for plotting the PV curves.

distributed with a start frequency 100 Hz and an end frequency 25 kHz which is one half the switching frequency. The used amplitude of the perturbation is $d = 0.01$ and the steady-state duty cycle is $D = 0.3196$. The AC analysis was performed by using the nonlinear model of the PV generator. The temperature was kept constant and the irradiance was changed between in the range (200, 1000) W/m^2 . The PV generator is TRINA PV module with an open circuit voltage around 50.1 V according to [34] with a maximum power of 395 W and a nominal MPP voltage of about 40.8 V and a nominal MPP current of approximately 9.69 A under standard test conditions. The specifications provided by the manufacturer for a single module are summarized in Table 2. More details can be found in [34].

The PV source is connected the DC-DC HIN high voltage gain boost converters which converts the DC PV voltage of about 40 V to the DC link voltage of about 380 V applied to a resistive load. Fig. 7 shows its $i-v$ curve for different values of irradiance $S \in (200, 1000) \text{ W}/\text{m}^2$ for temperature $\Theta = 25^\circ\text{C}$. The results were obtained by using the PSIM[®] schematic diagram depicted in Fig. 6. A ramp voltage was applied to the PV generator starting at zero and ending at a voltage larger than the open circuit voltage for each irradiance value. The power and the current of the PV generator are sensed and then plotted in terms of the PV voltage for the different irradiance levels. To have all the plots in the same figure, the parameter sweep facility of PSIM[®] was used.

TABLE 2 The parameter values of the PV source at standard weather conditions $S = 1000 \text{ W}/\text{m}^2$ and $\Theta = 25^\circ\text{C}$.

Parameter	Value
Number of series-connected cells in a module	72
Open-circuit voltage of a module V_{oc}	50.1 V
Short-circuit current I_{sc}	10.13 A
PV voltage at maximum power V_{mpp}	40.8 V
PV current at maximum power I_{mpp}	9.69 A
PV maximum power P_{mpp}	395 W

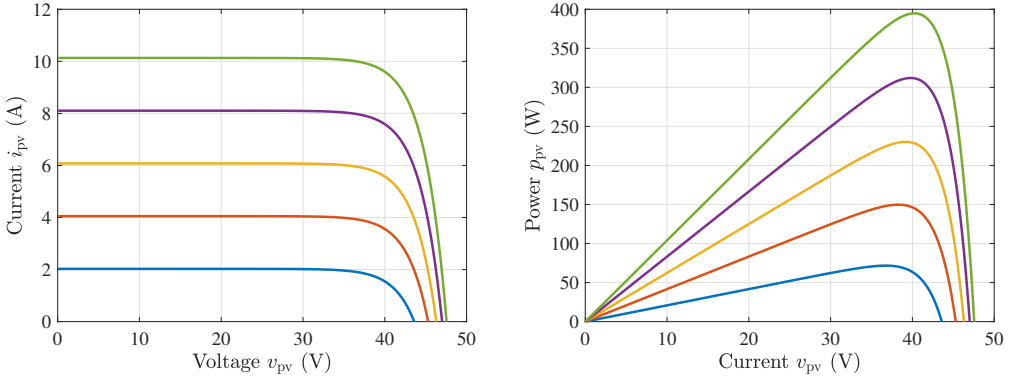


FIGURE 7 The PV curves for different values of the irradiance S between 200 W/m^2 ($P_{\text{mpp}} \approx 70 \text{ W}$) and 1000 W/m^2 ($P_{\text{mpp}} \approx 395 \text{ W}$). $\Theta = 25 \text{ }^\circ\text{C}$.

TABLE 3 The used parameters for the HIN converter power stage.

Parameter	f_s	L_1, L_2	C_1, C_2, C_3, C_4	C_{pv}	R
Value	50 kHz	200 μH	10 μF	100 μF	378-795 Ω

4.2 | PV voltage type-III controller design

Another key feature with PSIM[®] software is that it is possible to perform AC sweep along with parametric sweep. Hence these features are both used to obtain the frequency response of the HIN converter for different irradiance levels. As in obtaining the PV curves, to have all the plots in the same figure, the parameter sweep facility of PSIM[®] must be used. Using the obtained frequency responses, the PV voltage control design can be performed by appropriately selecting the required performances with regard to settling time, crossover frequency and phase margin under all weather conditions. Although the design can be obtained using a mathematical model, this is a complex task even for reduced order and conventional topologies of these converters. The complexity increases much when the order of the converter become high and it is fed from nonlinear sources like a PV generator. Using computer-aided design (CAD) tools like PSIM[®] significantly reduces the design task and its time of development. A useful tool that comes with PSIM[®] software is `smartCtrl` which allows the control design of switching converters without the need of a mathematical model nor the operating mode. Once the frequency response of the converter is obtained by using the AC sweep, the result can be used by `smartCtrl` which after introducing the desired crossover frequency and the phase margin in a suitable solution map and specifying the switching frequency, the desired output voltage and the type of the controller to be used, it shows its corresponding Bode and Nyquist diagrams together with the transient time response while providing the component values needed to implement the specified controller as well as the voltage divider resistors. The provided component values can be used to test the performances of the converter in the time domain by performing PSIM[®] simulations. This procedure will be used here to design a controller for the input PV voltage of the HIN converter.

A type-III controller can be used for boosting the phase by 180° and for getting a zero steady-state error. The gain, the poles and the zeros of the controller can be selected according to the desired crossover frequency and phase margin of the system. This controller can be implemented by using the circuit diagram shown in Fig. 8. Its transfer

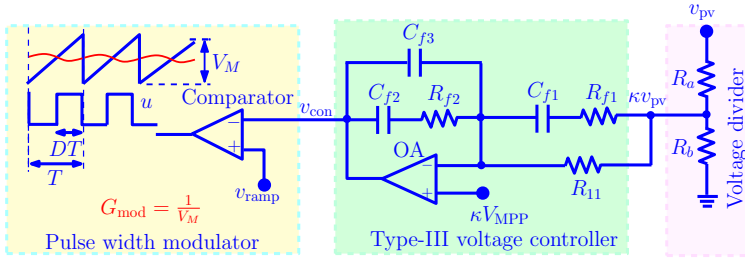


FIGURE 8 Circuit diagram for implementing a type-III controller.

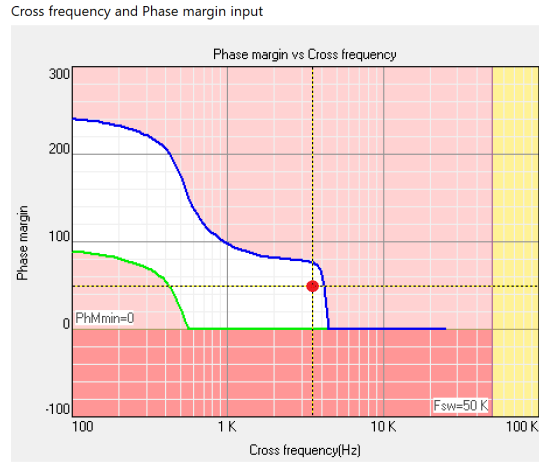


FIGURE 9 The solution map of the HIN converter with a type-III controller for irradiance $S = 1000 \text{ W/m}^2$, $\Theta = 25 \text{ }^\circ\text{C}$ ($P_{\text{mpp}} \approx 490 \text{ W}$) and $R = 378 \text{ } \Omega$. The selected design point corresponds to a crossover frequency $f_c = 3.5 \text{ kHz}$ and a phase margin $\varphi_m = 50^\circ$.

function can be expressed as follows [35]:

$$H_c(s) = -\frac{R_{11} + R_{f1}}{R_{11}R_{f1}C_{f3}} \frac{\left(s + \frac{1}{R_{f2}C_{f2}}\right)\left(s + \frac{1}{(R_{11} + R_{f1})C_{f1}}\right)}{s\left(s + \frac{C_{f1} + C_{f3}}{R_{f2}(C_{f1}C_{f3})}\right)\left(s + \frac{1}{R_{f1}C_{f1}}\right)} \quad (7)$$

The poles and zeros of the type-III controller and the values of the passive components to implement it will be provided by `SmartCtrl` tool of PSIM[®]. With this tool the design becomes simple because an accurate mathematical

TABLE 4 The provided component values by `SmartCtrl` for the voltage divider and type-III controller.

Parameter	R_a	R_b	R_{11}	R_{f1}	R_{f2}	C_{f1}	C_{f2}	C_{f3}
Value	1.18 k Ω	30.31 Ω	10 k Ω	618.45	7.66 k Ω	17.74 nF	24.59 nF	1.52 nF

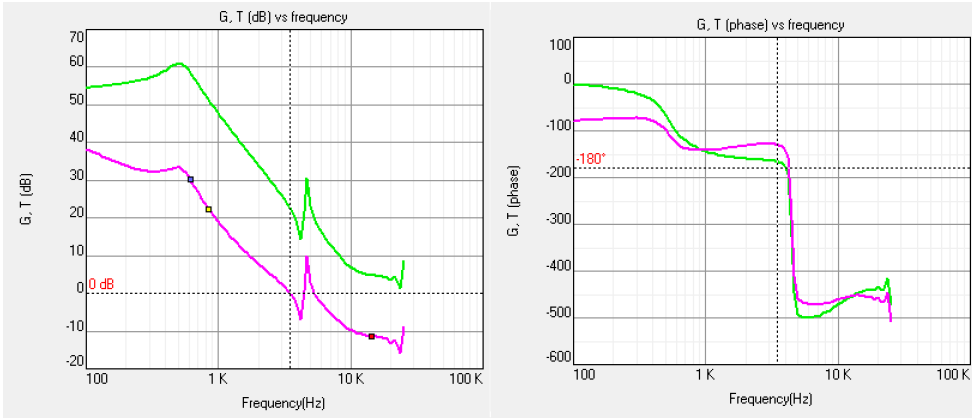


FIGURE 10 The d -to- v_{pv} frequency response of the HIN converter power stage and of the total loop using a type-III controller with desired crossover frequency and phase margin for irradiance $S = 1000 \text{ W/m}^2$ ($P_{mpp} \approx 490 \text{ W}$), $R = 378 \Omega$ and $\Theta = 25 \text{ }^\circ\text{C}$. Left: Amplitude. Right: Phase.

model is not necessary while an accurate frequency response from the switched model valid up to one half switching converter can be easily obtained by performing AC sweep. First the frequency response corresponding of the PV-fed HIN converter is obtained using AC sweep with the parameter values depicted in Table 3 for the converter power stage and Tab2 for the PV source with irradiance level $S = 1000 \text{ W/m}^2$ and temperature $\Theta = 25 \text{ }^\circ\text{C}$ ($P_{mpp} \approx 490 \text{ W}$). A phase margin of 50° and a crossover frequency $f_c \approx 3.5 \text{ kHz}$ were selected following the solution map of Fig. 9 which shows shows all the pairs f_c - φ_m in the specified frequency range in AC sweep. All the pairs within the white region generates a stable closed-loop system with the corresponding crossover frequency f_c and phase margin φ_m . Outside this region, the system will be unstable.

The frequency response of the open loop HIN converter and the total loop gain by taking including the type-III controller with the desired design specification in terms of crossover frequency and phase margin are shown in Fig. 10. It has been observed from different numerical simulations that for most values of the irradiance and temperature, a crossover frequency between 3 kHz and 4 kHz and a phase margin above 45° can always be selected in the solution map. Once a point defining the crossover frequency and the phase margin in the solution map is selected, `SmartCtrl1` will provide the component values needed to implement the type-III controller and the voltage divider resistors according to the scheme shown in Fig. 8. The selected pulse width modulator gain G_{mod} is unity. The selected gain of the voltage divider for PV voltage sensing is $\kappa := R_a / (R_a + R_b) = 1/40 = 0.025$. By selecting this divider gain and $R_{11} = 10 \text{ k}\Omega$, the rest of component values provided by `SmartCtrl1` are depicted in Table 4. These values are used in the type-III controller whose output is used as an input to a comparator. The other input to the comparator is a sawtooth signal v_{ramp} with amplitude $V_M = 1 \text{ V}$ and frequency 50 kHz. The driving signal u for the switches S_1 and S_2 is the output of the comparator according the scheme of Fig. 8. The previous scheme and control parameter values will be used in the next section to test the performances of the converter by performing PSIM[®] simulations in the time domain.

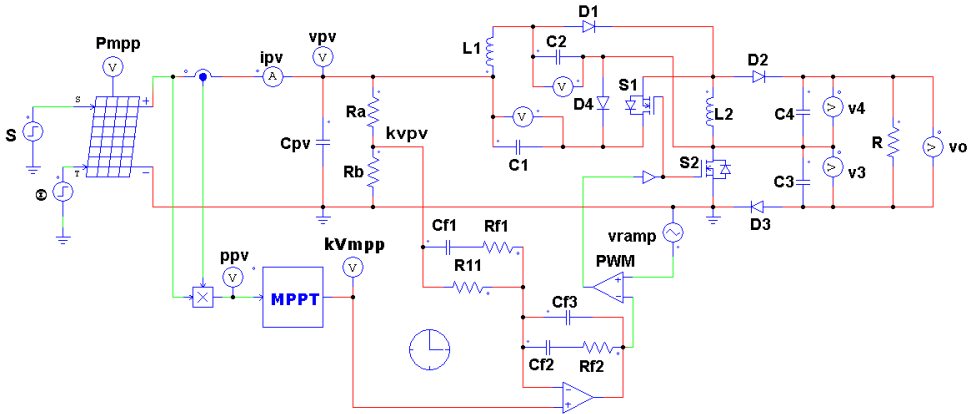


FIGURE 11 The PSIM[®] schematic diagram of the HIN converter under the type-III controller with an MPPT control.

5 | TIME DOMAIN SIMULATIONS

The complete PSIM schematic is depicted in Fig. 11 together with the content of the parameters file that PSIM[®] uses for performing the simulations. The converter control system uses a single loop control dealing only with the PV voltage. The controller design was performed according to the results presented in the previous section and the parameter values are provided by `smartCtrl1`. As can be observed, a type-III controller is used to control the PV voltage to its desired value which is provided by an MPPT block. The goal of MPPT is to seek the operating PV voltage and current that maximizes its power output as weather conditions vary. This is accomplished by varying the reference voltage provided by the MPPT algorithm as a function of the irradiance level and temperature. The reference signal provided by the MPPT is a scaled value of the voltage at the maximum power point and is provided by using Perturb and Observe algorithm. This algorithm periodically perturb the reference voltage with a fixed perturbation period T_{mpp} . The settling time of the converter after an MPPT perturbation must be enough smaller than the MPPT perturbation period T_{mpp} for ensuring robust stability and high efficiency of the algorithm. The MPPT algorithm can be degraded if the settling time is low. Therefore it is important to optimize this parameter. The sampling period of the MPPT controller has been chosen to be $T_{mpp} = 5$ ms which is enough larger than the settling time of the system due to a step change in the PV voltage reference V_{mpp} . The perturbation amplitude applied to V_{mpp} is $\Delta V_{mpp} = 1$ V ($\kappa \Delta V_{mpp} = 0.025$ V). The simulation is started with temperature $\Theta = 25$ °C and irradiance $S = 500$ W/m². The load resistance is adapted according to irradiance value in order to maintain the average output voltage at $V_o = 380$ V. Namely, for $S = 500$ W/m², $R = 795$ Ω and for $S = 1000$ W/m², $R = 378$ Ω .

PSIM[®] simulations are performed by using the schematic circuit diagram depicted in Fig. 11. The time-domain response of the complete system starting from zero initial conditions is depicted in Fig. 12. From $t = 0$ to $t = 0.25$ s, the PV system is operated with $S = 500$ W/m² and the corresponding maximum power is ($P_{mpp} \approx 190$ W). It is worth to note that the PV voltage is well regulated to its reference provided by the MMPT controller which is approximately 39 V. When the irradiance level changes, the input voltage V_{pv} undergoes a small change and after a short transient period it is regulated again to its new MPP voltage reference which is updated by the MPPT controller. Therefore, the type-III controller is capable of making the converter to track the voltage reference V_{pv} . The settling time due MPPT perturbations is much smaller than the MPPT perturbation period as desired. The operating duty cycle at the MPP is

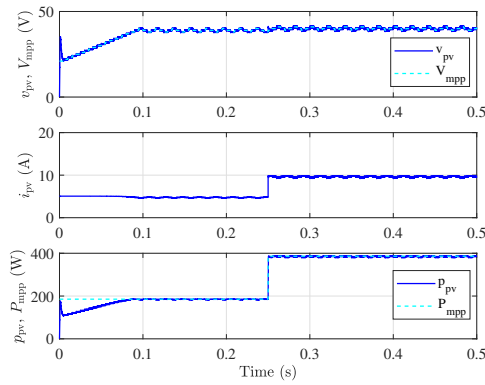


FIGURE 12 The response of the PV voltage for the HIN boost converter with the type-III input voltage control during startup and under irradiance step change between $S = 500 \text{ W/m}^2$ ($P_{mpp} \approx 190 \text{ W}$) and 1000 W/m^2 ($P_{mpp} \approx 395 \text{ W}$). $\Theta = 25 \text{ }^\circ\text{C}$. $R = 795 \text{ } \Omega$ for $S = 500 \text{ W/m}^2$ and $R = 378 \text{ } \Omega$ for $S = 1000 \text{ W/m}^2$.

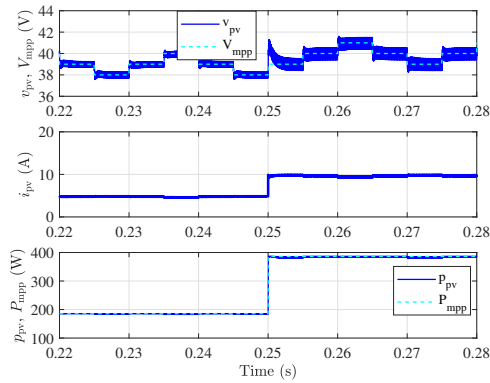


FIGURE 13 A close view of the response of the PV voltage for the HIN boost converter with the type-III input voltage control under irradiance step change between $S = 500 \text{ W/m}^2$ ($P_{mpp} \approx 189 \text{ W}$) and $S = 1000 \text{ W/m}^2$ ($P_{mpp} \approx 395 \text{ W}$). $\Theta = 25 \text{ }^\circ\text{C}$. $R = 795 \text{ } \Omega$ for $S = 500 \text{ W/m}^2$ and $R = 378 \text{ } \Omega$ for $S = 1000 \text{ W/m}^2$.

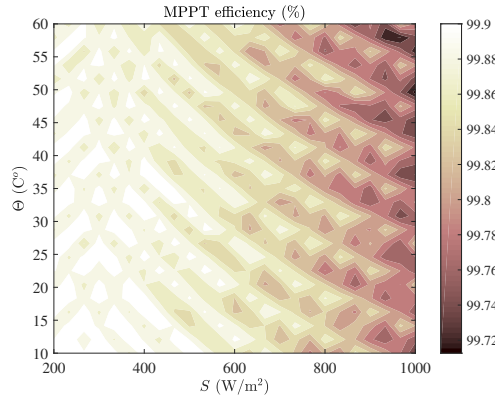


FIGURE 14 The MPPT efficiency as a two-dimensional function of the temperature and irradiance.

$D_{\text{mpp}} \approx 0.3196$ which is not excessively large differently to other switching converters ($M(0.3196) = 380/40.8 = 9.31$). The results demonstrate that the designed system is capable to operate at the optimum operating point regardless of the value of the irradiance.

Fig. 13 shows a close view of the steady-state response of the system where the PV voltage and its reference, the extracted the power p_{pv} from the PV source and its maximum power P_{mpp} are represented, when irradiance level change from $S = 500 \text{ W/m}^2$ ($P_{\text{mpp}} \approx 189 \text{ W}$) to $S = 1000 \text{ W/m}^2$ ($P_{\text{mpp}} \approx 395 \text{ W}$). It is worth noticing that the reference voltage V_{mpp} dictated by the MPPT controller oscillates between the values dictated by the MPPT control with a sampling period $T_{\text{mppt}} = 5 \text{ ms}$ and a perturbation amplitude $\Delta V_{\text{mpp}} = 1 \text{ V}$.

The ratio between the averaged harvested power \bar{p}_{pv} and the maximum available power P_{mpp} was used to calculate the MPPT efficiency. Fig. 14 shows the tracking efficiency $\eta = 100\bar{p}_{\text{pv}}/P_{\text{mpp}}$ as a two-dimensional function of the irradiance and temperature. Note that over most of the selected range of temperature and irradiance values, the tracking efficiency η remains better than 99.72% .

The steady-state inductor current i_1 and i_2 and the capacitor voltages v_1 , v_2 , v_3 , and v_4 and the output voltage v_o are shown in Fig. 15 for $S = 500 \text{ W/m}^2$ and for $S = 1000 \text{ W/m}^2$. It is worth to note that the steady-state averaged values of the state variables of the HIN converter (capacitor voltages and the inductor currents) are in a good agreement with the theoretical predictions given in Section 3. For instance, for $S = 500 \text{ W/m}^2$ and $R = 795 \Omega$, the average output voltage is $V_o \approx 380 \text{ V}$, the MPP voltage is $V_{\text{mpp}} \approx 38.85 \text{ V}$ and the duty cycle is $D \approx 0.3215$, the voltage conversion gain is $M(0.3215) \approx 9.78$ and according to the steady-state analysis in Section 3, one has $I_1 \approx 4.67 \text{ A}$, $I_2 \approx 6.88 \text{ A}$, $V_1 \approx 147 \text{ V}$, $V_2 \approx 89 \text{ V}$, $V_3 \approx 190 \text{ V}$ and $V_4 \approx 190 \text{ V}$. The theoretical values of the inductor current ripples are $\Delta i_1 = 4.15 \text{ A}$ and $\Delta i_2 = 6.11 \text{ A}$. All these theoretical results are in perfect agreement with the values obtained from PSIM[®] numerical simulations depicted in Fig. 15. For $S = 1000 \text{ W/m}^2$ and $R = 378 \Omega$, the same average output voltage is maintained $V_o \approx 380 \text{ V}$, the MPP voltage is $V_{\text{mpp}} \approx 40.5 \text{ V}$ and the duty cycle is $D \approx 0.3187$ ($M(0.3187) \approx 9.4$) and according to the steady-state analysis in Section 3, one has $I_1 \approx 9.41 \text{ A}$, $I_2 \approx 13.82 \text{ A}$, $V_1 \approx 149 \text{ V}$, $V_2 \approx 89 \text{ V}$, $V_3 \approx 190 \text{ V}$ and $V_4 \approx 190 \text{ V}$. These theoretical results are also in a remarkable agreement with the PSIM[®] simulations results depicted in Fig. 15.

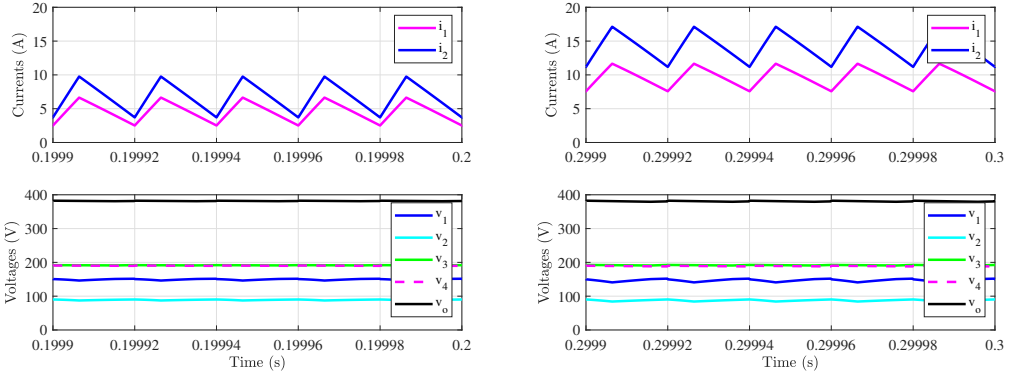


FIGURE 15 Steady-state waveforms of the HIN converter state variables, i_1 , i_2 , v_1 , v_2 , v_3 , v_4 and v_o for $S = 500 \text{ W/m}^2$ and $R = 795 \Omega$ (left) and irradiance $S = 1000 \text{ W/m}^2$ and $R = 378 \Omega$ (right). $\Theta = 25^\circ \text{ C}$

6 | CONCLUSIONS

In this paper, small signal modeling and control design for a high voltage gain HIN converter when used in a PV system has been addressed using PSIM[®] software. A simple single loop voltage mode control strategy was employed resulting in a easy to implement MPPT control without a requirement for a mathematical modeling of the entire system. The dynamic performances was presented in terms of varying irradiance and accordingly the controller parameter were chosen to achieve an optimum system response in terms of settling time, overshoot and MPPT tracking stability and efficiency. The designed PV system was tested under steady state operation and under rapidly changing weather conditions. The converter offers the possibility of an optimum regulation of the PV voltage with voltage mode control using a type-III compensation network resulting in a low overshoot, a short settling time and a negligible energy loss after a step change of input PV voltage reference due to the maximum power point tracking (MPPT) perturbation or to irradiance change. PSIM[®] model of the PV source connected to the high voltage gain HIN boost converter was used for performing numerical simulations and the results demonstrated that the HIN converter could be an excellent candidate for simple MPPT tracking in PV systems requiring high voltage gain. In particular, the simulation results have shown that the designed system is characterized by a fast convergence to the maximum power point of the PV system during steady-state regime and under rapid changes in the weather conditions.

Acknowledgments

This work was supported by the Spanish *Ministerio de Economía y Competitividad* under grants DPI2013-47293-R. A. El Aroudi and M. Al-Numay extend their appreciation to the International Scientific Partnership Program ISPP at King Saud University for funding this research work through ISPP#2020.

References

- [1] Liu H., Hu H., Wu H., Xing Y., and Batarseh I., "Overview of high-step-up coupled-inductor boost converters," *IEEE Journal of Emerging & Selected Topics in Power Electronics*, vol. 4, no. 2, pp. 689–704, 2016.
- [2] Varesi, K, Hassanpour, N, Saeidabadi, S. Novel high step-up DC–DC converter with increased voltage gain per devices

- and continuous input current suitable for DC microgrid applications. *Int J Circ Theor Appl.* 2020; 48: 1820– 1837.
- [3] Zhang, G, Chen, H, Yu, S, et al. An extendable single-switch n-cell boost converter with high voltage gain and low components stress for renewable energy. *Int J Circ Theor Appl.* 2020; 48: 817– 831.
- [4] Mohammadi, F, Farhadi-Kangarlu, M, Rastegar, H, Khorsandi, A, Pichan, M. P-type non-isolated boost DC-DC converter with high voltage gain and extensibility for DC microgrid applications. *Int J Circ Theor Appl.* 2019; 47: 1812– 1836.
- [5] Rosas-Caro J., Mancilla-David F., Mayo-Maldonado J., Gonzalez-Lopez J., "A transformer-less high-gain boost converter with input current ripple cancelation at a selectable duty cycle," *IEEE Transactions on Industrial Electronics*, vol. 60, no. 10, pp. 4492–4499, 2013.
- [6] Yang P., Xu J., Zhou G., and Zhang S., "A new quadratic boost converter with high voltage step-up ratio and reduced voltage stress," in *Power Electronics & Motion Control Conference*, 2012.
- [7] Pires V. F., Cordeiro A., Foito D., and Silva J. F., "High step-up DC-DC converter for fuel cell vehicles based on merged quadratic boost-Cuk," *IEEE Transactions on Vehicular Technology*, vol. 68, no. 8, pp. 7521–7530, 2019.
- [8] Rosas-Caro J. C., Ramirez J. M., Peng F. Z., and A. Valderrabano, "A DC-DC multilevel boost converter," *IET Power Electronics*, vol. 3, no. 1, pp. 129–137, 2010.
- [9] Zhu B., Wang H., and vilathgamuwa H., "Single switch high step-up boost converter based on a novel voltage multiplier," *IET Power Electronics*, vol. 12, no. 14, 2019.
- [10] Zhu X., Zhang B., Li Z., Li H., and Ran L., "Extended switched-boost DC-DC converters adopting switched-capacitor/switched-inductor cells for high step-up conversion," *IEEE Journal of Emerging & Selected Topics in Power Electronics*, pp. 1–1, 2016.
- [11] Poorali B. and Adib E. , "Soft-switched high step-up quasi-z-source dc-dc converter," *IEEE Transactions on Industrial Electronics*, vol. 67, no. 6, pp. 4547–4555, 2020.
- [12] Li W. and He X., "ZVT interleaved boost converters for high-efficiency, high step-up DC-DC conversion," *IET Electric Power Applications*, vol. 1, no. 2, pp. 284–290, 2007.
- [13] Zhao Y., Li W., Deng Y., and He X., "High step-up boost converter with passive lossless clamp circuit for non-isolated high step-up applications," *IET Power Electronics*, vol. 4, no. 8, pp. 851–859, 2011.
- [14] Seong H., Kim H., Park K., Moon G., and Youn M., "High step-up DC-DC converters using zero-voltage switching boost integration technique and light-load frequency modulation control," *IEEE Transactions on Power Electronics*, vol. 27, no. 3, pp. 1383–1400, 2012.
- [15] Henn G. A. L., Silva R. N. A. L, Praça P. P., L. H., Barreto S. C., and Oliveira D. S., "Interleaved-boost converter with high voltage gain," *IEEE Transactions on Power Electronics*, vol. 25, no. 11, pp. 2753–2761, 2010.
- [16] Hu X., Ma P., Wang J., Tan G., and Yao Z., "A hybrid cascaded DC-DC boost converter with ripple reduction and large conversion ratio," *IEEE Journal of Emerging and Selected Topics in Power Electronics*, 2019.
- [17] Peng F. Z., "Z-source inverter," *IEEE Transactions on Industry Applications*, vol. 39, no. 2, pp. 504-510, March-April 2003.
- [18] Siwakoti Y. P. , Peng F. Z., Blaabjerg F., Loh P. C., and Town G. E., "Impedance source network for electric power conversion—Part I: A topological review," *IEEE Trans. Power Electron.*, vol. 30, no. 2, pp. 699–716, Feb. 2015.
- [19] Siwakoti Y. P., Blaabjerg F., and Loh P. C., "New magnetically coupled impedance (Z-) Source networks," *IEEE Trans. Power Electron.*, vol. 31, no. 11, pp. 7419–7435, Jun. 2015.
- [20] Chub A., Vinnikov D., Blaabjerg F., and Peng F. Z., "A review of galvanically isolated impedance-source DC-DC converters," *IEEE Trans. Power Electron.*, vol. 31, no. 4, pp. 2808–2828, Apr. 2016.

- [21] Qian W., Peng F. Z., and Cha H., "Trans-Z-source converters," *IEEE Trans. Power Electron.*, vol. 26, no. 12, pp. 3453–3463, Dec. 2011.
- [22] Nguyen M. K., Lim Y. C., and Kim Y. G., "TZ-source converters," *IEEE Trans. Ind. Electron.*, vol. 60, no. 12, pp. 5686–5695, Dec. 2013.
- [23] Adamowicz M., Strzelecki R., Peng F. Z., Guzinski J., and Abu-Rub H., "New type LCCT-Z-source converters," in *Proc. Eur. Conf. Power Electron. Appl.*, Sep. 2011, pp. 1–10.
- [24] Loh P. C., Li D., and Blaabjerg F., "Γ-Z-source converters," *IEEE Trans. Power Electron.*, vol. 28, no. 11, pp. 4880–4884, Nov. 2013.
- [25] Strzelecki R., Adamowicz M., Strzelecka N., and Bury W., "New type T-source converter," in *Proc. Compat. Power Electron.*, May 2009, pp. 191–195.
- [26] Siwakoti Y. P., Loh P. C., Blaabjerg F., Andreasen S. J. and Town G. E., "Y source impedance network based boost DC/DC converter for distributed generation," *IEEE Trans. Ind. Electron.*, vol. 62, no. 2, pp. 1059–1069, Feb. 2015.
- [27] Ayachit A., Siwakoti Y. P., Galigekere V. P. N., Kazimierczuk M. K. and Blaabjerg F., "Steady-State and Small-Signal Analysis of A-Source Converter," *IEEE Transactions on Power Electronics*, vol. 33, no. 8, pp. 7118–7131, Aug. 2018.
- [28] Zhang, G, Chen, W, Yu, SS, El Aroudi, A. Hourglass-shaped impedance network based nonelectrolytic capacitors high step-up converter with low voltage stress. *Int J Circ Theor Appl*. 2020; 1– 17. <https://doi.org/10.1002/cta.2904>
- [29] Available online: <https://powersimtech.com/products/psim/> (accessed on 22 February 2021).
- [30] B. Wu, S. Li, K. Ma Smedley, and S. Singer, "A family of two-switch boosting switched-capacitor converters," *IEEE Transactions on Power Electronics*, vol. 30, no. 10, pp. 5413–5424, 2015.
- [31] K. Shiluveru, A. Singh, A. Ahmad, R. K. Singh, and A. R. Beig, "Switched capacitor embedded high gain impedance source dc-dc converter," in *IECON 2019 - 45th Annual Conference of the IEEE Industrial Electronics Society*, vol. 1, 2019, pp. 5045–5050.
- [32] J. Liu, J. Wu, J. Qiu, and J. Zeng, "Switched z-source/quasi-z-source dc-dc converters with reduced passive components for photovoltaic systems," *IEEE Access*, vol. 7, pp. 40 893–40 903, 2019.
- [33] K. Patidar and A. C. Umarikar, "High step-up pulse-width modulation dc-dc converter based on quasi-z-source topology," *IET Power Electronics*, vol. 8, no. 4, pp. 477–488, 2015.
- [34] Available online: <http://static.trinasolar.com> (accessed on 22 February 2021).
- [35] Mattingly, D. *Designing Stable Compensation Networks for Single Phase Voltage Mode Buck Regulators*; Technical Brief; Intersil: Milpitas, CA, USA, 2003